



## OPEN Seasonal and interannual variations in material transport in the Korea Strait originating from the Taiwan Strait

Seung-Tae Lee<sup>1</sup>, Yong-Yub Kim<sup>2,3</sup>✉, Yong-Jin Tak<sup>4</sup>✉, Seunghwa Chae<sup>5</sup> & Yang-Ki Cho<sup>5</sup>

Understanding the variability in material transport from the Taiwan Strait (TS) to the Korean Strait (KS) is crucial for predicting ecological changes and the spread of marine debris in the East Asian Marginal Seas (EAMS). However, the dynamic variability of this transport remains poorly understood. In this study, we investigated the dynamic variability of material transport from the TS to the KS, using a Lagrangian particle-tracking system coupled with a three-dimensional numerical model. The model results showed that particles originating from the TS most frequently passed through the KS in August, with distinct interannual variability. Our findings indicate that southerly winds enhance the sea surface height (SSH) gradient in the southwestern East China Sea (ECS) shelf region through surface Ekman transport, weakening cross-shelf offshore currents and preventing particles from being transported offshore. The interannual variability of southerly winds is associated with variations in SSH in the southwestern shelf region, thereby modulating material transport from the TS to the KS. Furthermore, southerly winds over the EAMS are found to strengthen during negative phases of the Pacific Decadal Oscillation, suggesting a potential linkage between material connectivity in the EAMS and large-scale climate indices. These findings reveal how physical processes govern material transport in the EAMS, offering valuable insights into the prediction of nutrient fluxes and pollutant dispersion.

The Korea Strait (KS), located between Kyushu Island and the Korean Peninsula, connects the East China Sea (ECS) and East/Japan Sea (EJS). The depth becomes shallow from the ECS to the KS but deep from the KS to the EJS<sup>1</sup>. The Tsushima Warm Current (TSWC) flows into the East/Japan Sea (EJS) throughout the year and is crucial in transporting relatively high-temperature and high-salinity water masses rich in organic and inorganic nutrients to higher latitudes<sup>2–5</sup>. These variations in the physical and biochemical properties of the TSWC significantly affect the ecosystem<sup>6</sup> and fishery production in the EJS<sup>7–9</sup> with increasing water temperatures presenting potential risks, particularly for large fish species<sup>10</sup>. During the summer of 2024, the National Institute of Fisheries Science (NIFS) reported unprecedented blooms of *N. nomurai* around the Korean Peninsula, which caused substantial damage to fisheries and marine ecosystems<sup>11</sup>. Therefore, investigating the origin and variability of the TSWC flowing through the KS is essential from both physical and ecological perspectives to understand the ecosystem in the EJS.

Previous studies on the origins of the TSWC have indicated that its primary sources include the Kuroshio intrusion crossing the continental slope in the ECS toward the marginal sea and the Taiwan warm current (TWWC) flowing along the ECS shelf (Fig. 1a)<sup>12,13</sup>. The TWWC exhibits strong seasonality, primarily influenced by monsoon winds rather than surface heat fluxes, with an annual mean transport volume of approximately 2 Sv<sup>13,14</sup> (Supplementary Fig. 1a,b). Through the numerical experiments, Kuroshio intrusion accounts for 83% of the TSWC transport in winter, whereas the TWWC contributes 66% in summer<sup>13,15</sup>. The Kuroshio intrusion contributes approximately 34% to the Taiwan Strait Warm Current (TSWC) in summer, while the Taiwan Warm Current (TWWC) contributes around 17% to the TSWC transport in winter<sup>15</sup>. Although previous studies have highlighted the contributions of the TWWC to the TSWC, the temporal variation in connectivity between the TSWC and TWWC, particularly regarding material transport, has not been comprehensively elucidated.

<sup>1</sup>Ocean Circulation and Climate Research Department, Korea Institute of Ocean Science and Technology, Busan, Republic of Korea. <sup>2</sup>Center for Climate Physics, Institute for Basic Science, Busan, Republic of Korea. <sup>3</sup>Pusan National University, Busan, Republic of Korea. <sup>4</sup>Department of Marine Ecology and Environment, Gangneung-Wonju National University, Gangneung, Republic of Korea. <sup>5</sup>School of Earth and Environmental Sciences/Research Institute of Oceanography, Seoul National University, Seoul, Republic of Korea. ✉email: kimyy308@pusan.ac.kr; yjtak@gwnu.ac.kr

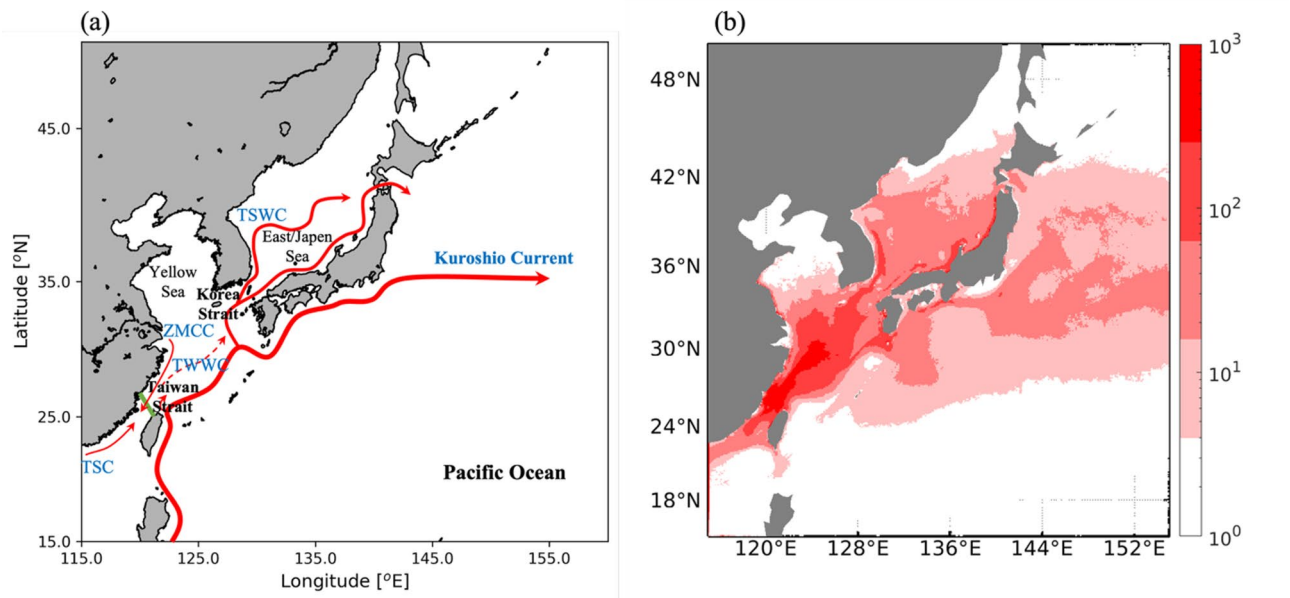


**Fig. 1.** Schematic diagram of study area. TSC, TWWC and TSWC represent the Taiwan Strait Current, Taiwan Warm Current, and Tsushima Warm Current. The green line represents the initial location of particles. **(b)** Mean horizontal distributions of particle trajectories from the Taiwan Strait from 1983 to 2019. Figures were generated by S-TLee using MATLAB R2024b (<http://www.mathworks.com>).

The Taiwan Strait (TS) is a channel with an average depth of 60 m between the coast of China and the island of Taiwan, connecting the South China Sea (SCS) and ECS<sup>13</sup>. The Taiwan Strait Current (TSC) that originates in the TS is influenced by the East Asia Monsoon, and in summer, it flows northwest at both the surface and subsurface levels owing to the influence of summer monsoon winds<sup>16,17</sup>. In contrast, in the winter, the surface water flows southward owing to the Zhe-min Coastal Current (ZMCC), which carries freshwater from the coast of China to the southwest, resulting in the formation of a front oriented in the east-west direction<sup>18,19</sup>. However, in winter, the subsurface experiences an upwind flow toward the northeast<sup>17</sup>.

As the TWWC primarily originates from the convergence of the TSC and the Kuroshio intrusion in the northeastern region of Taiwan Island<sup>20</sup> the water mass of the TS is important in influencing the water properties of the TSWC. Kim et al. (2014) suggested a strong connection between freshwater transport in the TS and KS, primarily in the subsurface of KS's eastern channel. They used freshwater as an index of water mass and showed a correlation between TS and KS; however, it had limitations regarding seasonal and interannual variability. In this study, we aimed to investigate how the path of the water mass from the TS changes seasonally and annually and identify the physical factors leading to these changes using three-dimensional numerical and Lagrangian trajectory models.

## Results and discussion

### Seasonal variation in the number of particles passing through from the TS to KS

Figure 1b illustrates the mean distribution of particle trajectories, where each particle was tracked for one year after its release, and the results were averaged over the entire period from 1983 to 2019, with releases originating from the TS. Particles from the TS moved northeast following the ocean currents. The particle trajectories originating from the TS predominantly traveled toward the KS and entered the EJS, whereas some dispersed offshore and were transported along the Kuroshio Current.

To examine the seasonal changes in particles traveling from the TS to KS clearly, the number of particles passing through the KS was counted based on their departure and arrival times from the TS. The average travel time of particles to reach the KS is about 5.7 months (Fig. 2a). Particles released during summer (JJA, 3.7 months) were more likely to reach the KS than those released in winter (DJF, 7 months), with the maximum departing in July. Particles departing in July required the shortest time of approximately 3 months to travel from TS to KS, whereas those departing in October required the longest time of approximately 8 months (Fig. 2c). Particles released from deeper layers in the TS were more likely to enter the KS than those released from the surface. (Supplementary Fig. 2a). The number of particles arriving from July to September was high, with most arriving in August (Fig. 2b). Particles arriving in June had the longest travel times, whereas those arriving in September had the shortest (Fig. 2d). Briefly, most particles departed in July and arrived quickly at the KS, with the highest number of particles arriving in August. These seasonal variations in travel time and number of particles are largely driven by the prevailing monsoonal wind patterns. During winter, the dominant northwesterly winds induce south and southwestward transport, carrying most particles toward the South China Sea. In contrast, summer southerly winds enhance northward and northeastward transport, facilitating more direct particle movement from the TS to the KS. These results indicate that the seasonal variability in travel time is tightly

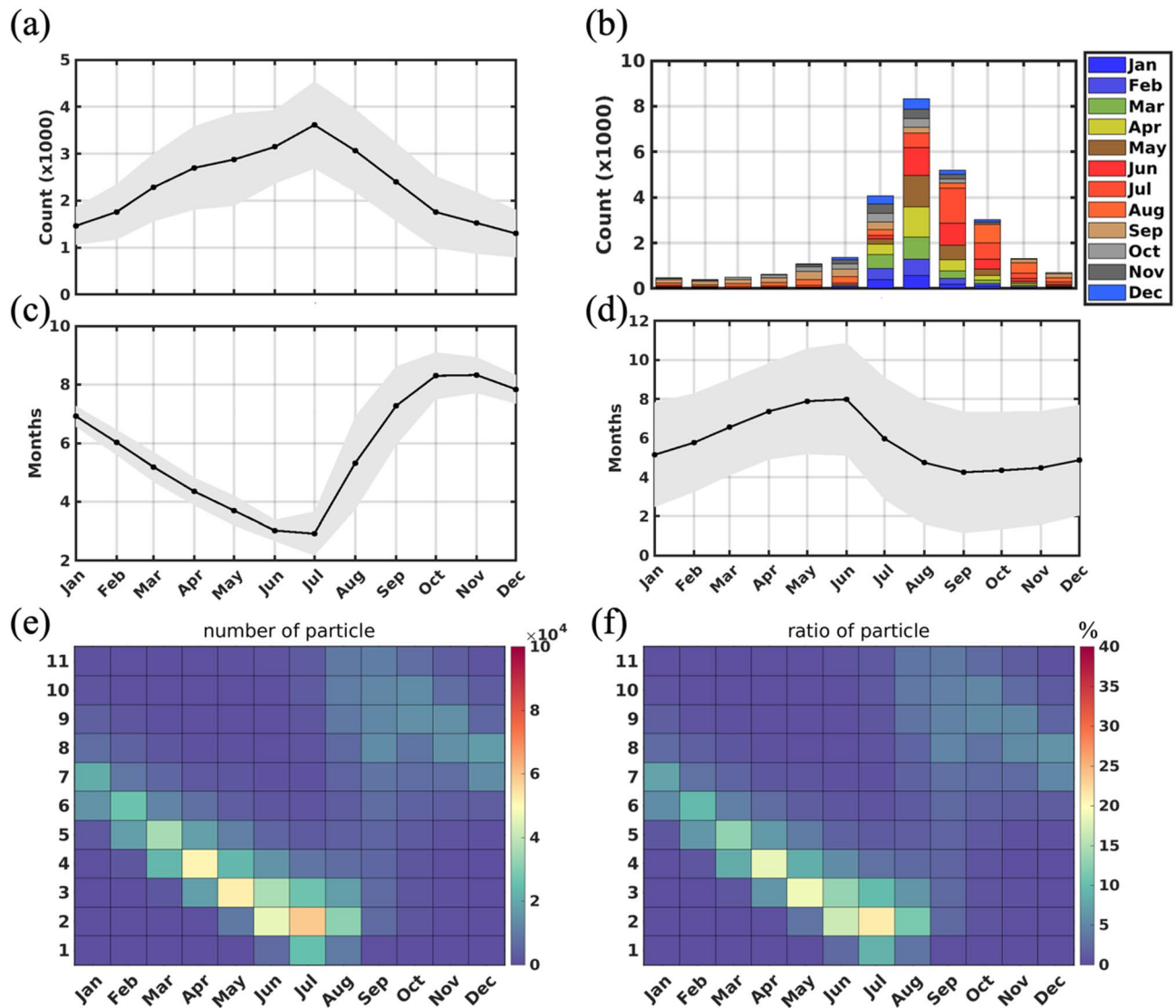


**Fig. 2.** Monthly mean time series of (a) the number of particles passing through the Korea Strait by departure month, and (b) stacked bar plot showing the number of particles arriving at the Korea Strait by month, with colors indicating release months from the Taiwan Strait, averaged from 1983 to 2019. (c, d) Monthly time series of average travel time of these particles, based on (a, c) the departure time from the Taiwan Strait and (b, d) the arrival time at the Korea Strait, averaged from 1983 to 2019. The red, blue, and black lines represent the particles that pass through the western, eastern channels of the Korea Strait, and the sum of both channels, respectively. Heatmaps for (e) the number of particles reaching the Korea Strait (f) and the ratio of particles from the Taiwan Strait to it reaching the Korea Strait. X- and Y-axes represent the release month and travel time (unit: month) of the particles, respectively. Figures were generated by S-TLee and Y-JTak using MATLAB R2024b (<http://www.mathworks.com>).

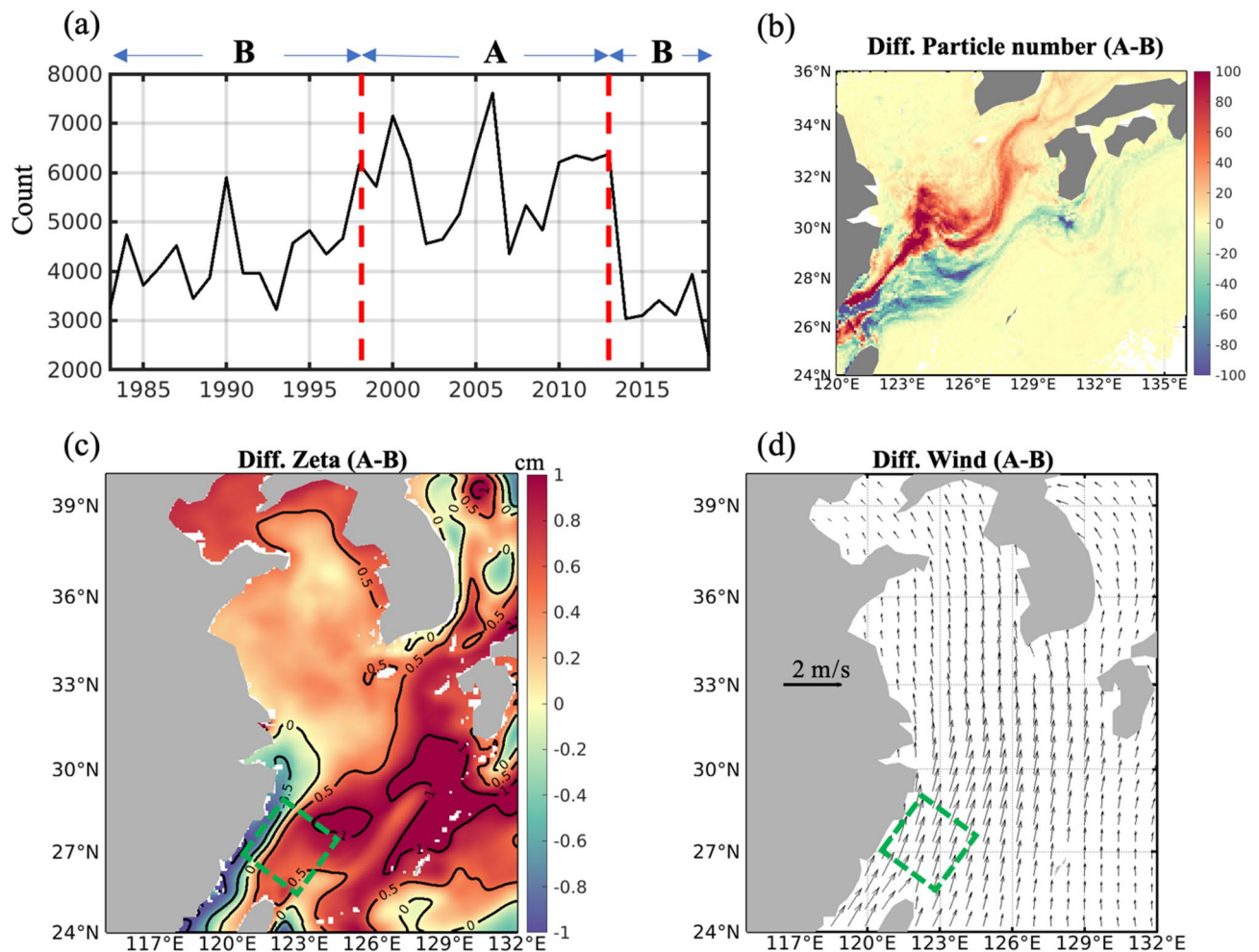
linked to surface wind-driven processes, highlighting the key role of monsoonal circulation in modulating particle connectivity between the TS and KS. More detailed process and associated interannual variations are discussed in next section “Effect of local wind on the interannual variability of the material transport from the TS to KS”.

Figure 2e,f show heatmaps of the number and ratio of particles originating from the TS that reached the KS. During winter, transport in the TS approaches 0 Sv owing to northerly winds<sup>16,22,23</sup> causing most particles to be diverted to the SCS. Consequently, less than 10% of the particles reached the KS. However, from March to August, the number of particles entering the KS increased to over 25% of the total particles released. Considering the travel time of the particles released each month, the particles released from January to July had the highest influx into the KS in July and August. This suggests that particles entering the ECS during winter and spring remain in the sea until summer, when changes in oceanic conditions facilitate their movement to the KS or offshore toward the Kuroshio Current.

### Effect of local wind on the interannual variability of the material transport from the TS to KS

Heatmap analysis underscored a new perspective, revealing that particles originating from the TS can remain in the ECS and later disperse simultaneously under the influence of physical oceanic conditions during summer. Considering the significant interannual variability in the number of particles entering the KS during summer (Fig. 2b), a composite analysis was conducted by dividing the data into two periods: Period A (1998–2013), representing the years with the highest influx, and Period B, comprising the remaining years (Fig. 3a), to examine the drivers of material transport. Figure 3a shows the time series of the number of particles originating from the TS and reaching the KS during summer (June–August). Figure 3c, d show the horizontal distributions of the differences between the high- and low-influx composite years for sea surface height (SSH) and wind during summer.

During Period A, southerly winds intensified over the southwestern ECS, spanning  $27^{\circ}$ – $29^{\circ}$  N meridionally and  $123^{\circ}$ – $125^{\circ}$  E zonally (Fig. 3d). This strong southerly wind drives surface particles northward and northeastward, contributing to an enhanced SSH gradient in this region compared to low-influx years (Fig. 3c). In high-influx years, the enhanced SSH gradient from wind was balanced by the Coriolis force, resulting in a northeastward geostrophic current. As geostrophic adjustment occurred faster than particle movement driven solely by Ekman transport, subsurface particles were transported toward the KS with the geostrophic current. Figure 4 shows the daily mean SSH and wind anomalies, including the locations of the particles in July 2000. On July 9, easterly wind anomalies relative to Period B were observed in the northeastern TS. The wind anomaly direction changed southerly on July 10, when the eastward SSH anomaly gradient increased. However, the change in the particle movement lagged behind that of the SSH distribution. The spatial SSH anomaly pattern persisted, preventing particles from moving eastward over regions with relatively high SSH anomalies and causing them to follow the SSH anomaly contours. Additionally, the onshore transport from the open sea was stronger during Period A



**Fig. 3.** (a) Time series of the number of particles passing the Korea Strait from Taiwan Strait from June to August. (b) The particle trajectory differences between high and low influx during Periods A and B composite years released from March to July. The horizontal distributions of the differences between the high and low influx composite years for (c) sea surface height (SSH) and (d) wind during summer. Green box is the area for the calculation of sea-level rise induced by the Ekman transport. Figures were generated by S-TLee using MATLAB R2024b (<http://www.mathworks.com>).

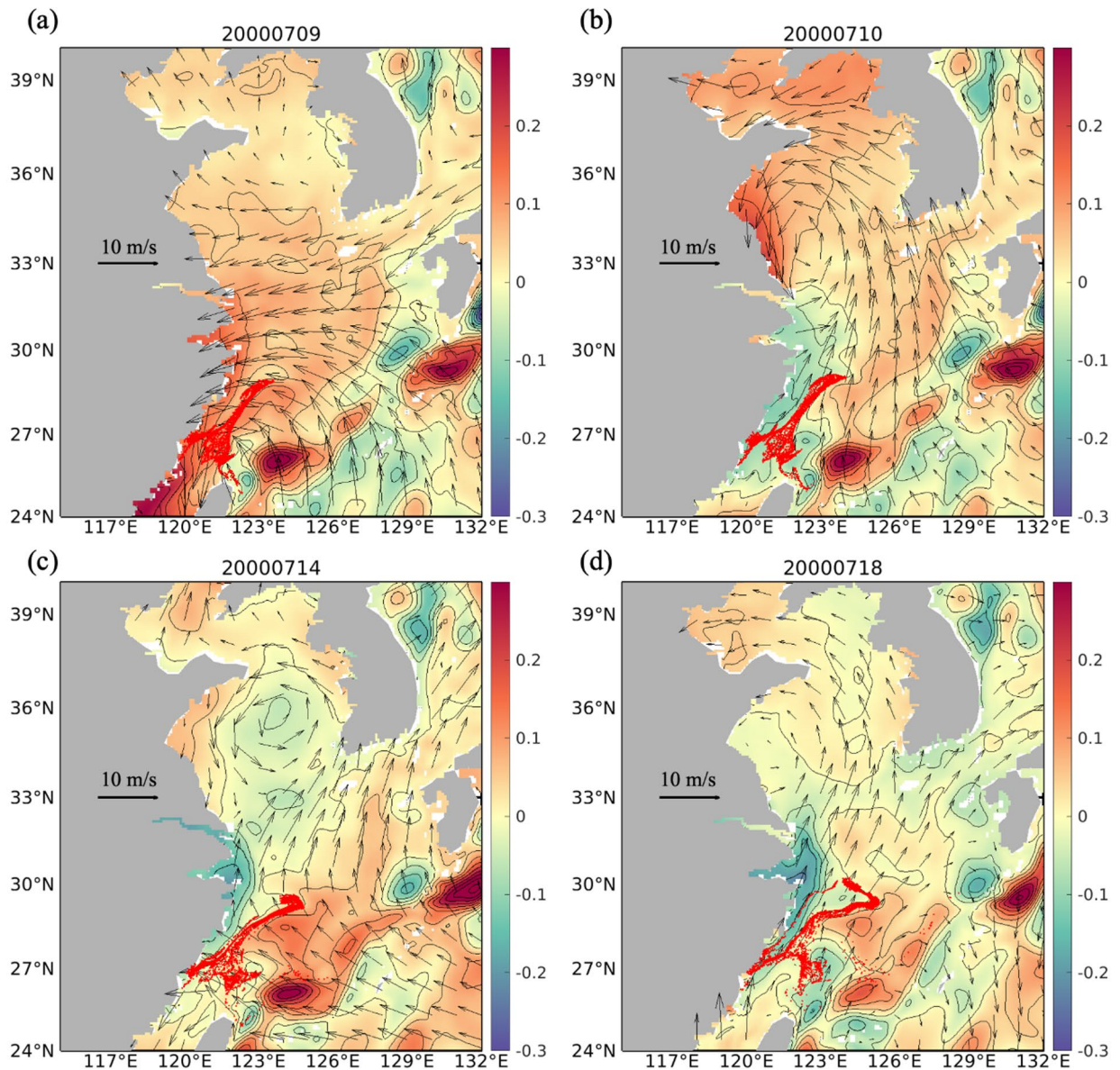


**Fig. 4.** Daily distribution of SSH and wind anomalies relative to Period B on (a) July 9, (b) July 10, (c) July 14, and (d) July 18. The SSH and wind anomalies were derived by subtracting the mean daily SSH and wind recorded during Period B. Red points represent the location of particles starting from the Taiwan Strait. Figures were generated by S-TLee using MATLAB R2024b (<http://www.mathworks.com>).

than that during Period B (Fig. 5). The interannual variability of the number of particles crossing the KS does not substantially differ depending on the initial release depths in the TS (Supplementary Fig. 2b).

Thus, the composite analysis and daily snapshots indicate that southerly winds enhanced the SSH gradient in this area through surface Ekman transport. This enhancement, combined with the alignment of wind direction and geostrophic current, prevented particles from being transported offshore and instead directed them toward the KS.

To analytically estimate the SSH difference caused by the variation in southerly wind stress between high- and low-wind years, the study area was simplified and the Ekman transport induced by wind stress was calculated as follows:

$$M = \frac{\tau}{\rho f}$$

where  $M$  is the Ekman transport ( $\text{m}^2/\text{s}$ ),  $\tau$  is the wind stress,  $\rho$  is the seawater density, and  $f$  is the Coriolis parameter. For simplicity, the calculation domain was set as a square box located northeast of the TS (green

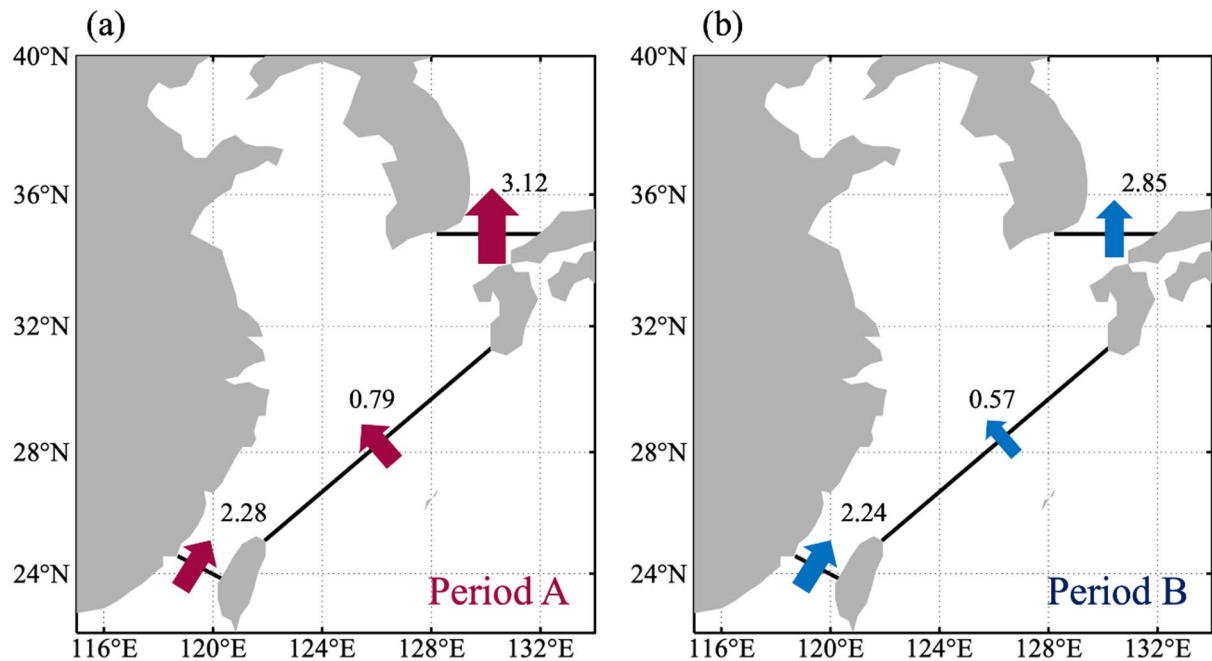


**Fig. 5.** Mean transport (Sv) through the Taiwan Strait, marginal shelf and Korea Strait during periods (A) and (B). The transport was averaged from June to August. Figures were generated by S-TLee and Schae using MATLAB R2024b (<http://www.mathworks.com>).

dashed box in Fig. 3c, d). The representative value for northeastward wind stress in this domain was set to  $0.006 \text{ N/m}^2$  from the model result (not shown here), with  $\rho$  taken as  $1025 \text{ kg/m}^3$  and the latitude set at  $27^\circ \text{ N}$ . Based on these values, the southeastward Ekman transport ( $M$ ) was estimated to be  $0.088 \text{ m}^2/\text{s}$ . The sea level rise ( $dh$ ) induced by Ekman transport over a square area with sides of  $300 \text{ km}$  over a period of  $1 \text{ d}$  was then computed using the following equation:

$$dh = \frac{M \cdot dx \cdot t}{(dx)^2}$$

where  $dx$  and  $t$  are  $300 \text{ km}$  and  $86,400 \text{ s}$ , respectively. Although the study area includes complex physical conditions, such as the Kuroshio Current, local topography, and baroclinicity, which may contribute to sea level variability, the computed sea level rise ( $dh$ ) was  $2.5 \text{ cm}$ , which closely corresponded to the sea level difference in the box area shown in Fig. 3c. This suggests that the Ekman transport induced by interannual variations in wind stress could contribute to sea level fluctuations in the region.

Figure 3b and Supplementary Fig. 3 show the trajectories of particles released from the TS during summer for the low- and high-influx composite years, as well as the differences between them. During the high-influx composite years, particles moved closer to the coast and flowed in northerly and northeasterly directions, resulting in reduced particle paths in the offshore transport region ( $27\text{--}29^\circ \text{ N}$ ,  $123\text{--}125^\circ \text{ E}$ ), whereas the eastward flow near  $29^\circ \text{ N}$  intensified. The southerly wind in this region could be a critical factor in determining the interannual variability in material connectivity between the TS and KS.

The empirical orthogonal function (EOF) results for the SSH and meridional wind stress during summer (June–August) from 1983 to 2019 confirmed the correlation among wind stress, SSH, and particles reaching the KS (Fig. 6). The first mode of EOF for the wind stress explained 59.8% of the total variance, and the eigenvector (Fig. 6a) was consistent with the pattern of the meridional wind stress in the composite analysis (Fig. 3d) over the southwestern ECS shelf region. The spatial pattern of the second mode for the SSH, with 12.3% of the variance, matched the pattern in the high-influx composite year (Fig. 6b). Moreover, the principal component time series of wind stress and SSH was significantly correlated with the number of particles reaching the KS (0.59 and 0.70, respectively). The principal component of wind stress was also strongly correlated with SSH (0.64), suggesting that the interannual variability of southerly winds over the ECS could be crucial in material transport from the TS to the KS by modulating SSH in the southwestern shelf region of the ECS. Incidentally, the eigenvector of the first mode of the SSH showed high variability near the Chinese coastal area, which could be linked to the freshwater discharge of the Changjiang River (Supplementary Fig. 4), with an insignificant correlation with the particles reaching the KS.

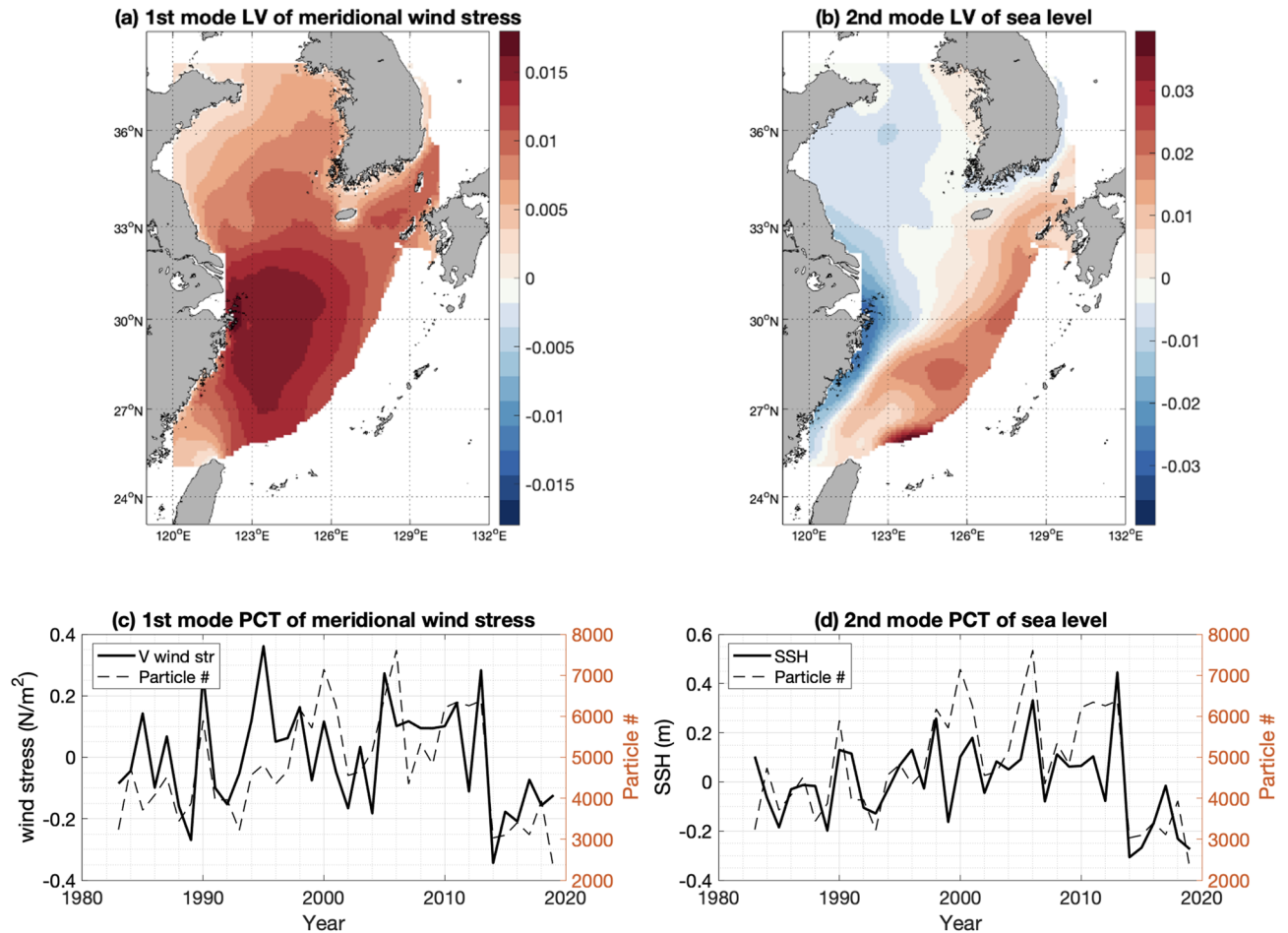


**Fig. 6.** Empirical orthogonal function (EOF) results over the ECS shelf (depth < 300 m) for the meridional wind stress (**a, b**) and sea level (**c, d**) during summer (June–August running mean) from 1983 to 2019. The variance explained by the first (second) leading EOF mode of meridional wind stress (sea level) was 59.8 (12.3) %. The first column (**a, c**) denotes the eigenvector (loading vector), and the second column shows the eigenvalue (principal component). The black dashed lines indicate the number of particles passing through the Korea Strait. Figures were generated by Y-YKim using MATLAB R2024b (<http://www.mathworks.com>).

The connectivity between the TS and KS is potentially influenced by broader decadal-scale variability. Supplementary Fig. 5 illustrates the time series of particles originating from the TS and passing through the KS from June to August, as well as the annual mean Pacific Decadal Oscillation (PDO) index. The two time series exhibited a strong negative correlation, with a correlation coefficient of -0.60. This indicates that the connectivity between the TS and KS increased during the negative phase of the PDO. The PDO is a key driver of decadal variability in the East Asian Summer Monsoon<sup>24</sup>. During the negative phase of the PDO, the sea level pressure distribution increased with southerly wind anomalies over the shelf region<sup>24–26</sup>. These enhanced southerly winds create SSH differences that prevent particles from escaping into the open sea, directing them northward. Consequently, connectivity between the straits could be enhanced during the negative phase of the PDO. However, climate indices, such as the PDO, are intricately linked to other indices, such as ENSO<sup>26–28</sup>. Therefore, further studies are required to investigate how climate-scale variability influences material connectivity in marginal seas.

## Conclusions

This study provided a comprehensive analysis of the material connectivity between the TS and KS using a three-dimensional numerical model and a Lagrangian trajectory model. The findings revealed significant seasonal and interannual variations influenced primarily by local wind conditions and surface Ekman transport in the ECS.

The study found pronounced seasonality in the connectivity between the TS and KS. In winter, the northerly winds significantly reduced transport in the TS, diverting most particles to the SCS and resulting in less than 10% reaching the KS, with a long travel time of approximately 7 months. From March to August, the number of particles entering the KS increased to over 25% of the total particles released. The influx peaks in July and August indicated that particles remained in the ECS during winter and spring and later moved to the KS simultaneously during summer. Material transport to the KS was strongly connected to the TS during summer (June to August),

suggesting that the physical conditions during summer could be critical factors in the connectivity between the KS and TS.

A composite analysis of years with high and low particle influx into the KS showed that stronger southerly winds during high-influx years could enhance the eastward surface Ekman transport, resulting in a steeper SSH gradient in the southwestern ECS shelf. This higher SSH gradient establishes a northeastward geostrophic current that directs particles northeastward along the ECS shelf, preventing them from being transported offshore. EOF analysis demonstrated a significant positive relationship among wind stress, SSH, and the number of particles reaching the KS during summer, indicating that the interannual variability in southerly winds over the ECS is crucial in modulating material transport from the TS to KS. The difference in particle paths highlights the role of southerly wind variability in modulating transport from the TS to KS, with particles in high-influx years driven further northward by relatively stronger southerly winds. Understanding the dynamics of material connectivity between the TS and KS is crucial for forecasting ecological changes and managing environmental impacts in the ECS and adjacent marginal seas. Although local winds appear to have a primary influence on the connectivity between the TS and KS, other factors, such as the discharge of low-salinity water from the Changjiang River and signals from the open ocean, such as the PDO variability, may also be crucial in connectivity. Assessing the contribution of these additional factors will further improve our understanding of the connectivity between the TS and KS. Future research should aim to refine these models and explore the impacts of climate change on these transport processes.

## Methods

### Regional three-dimensional numerical model

This study used the Regional Ocean Modeling System (ROMS) version 4.0, which is a numerical model of ocean circulation in three dimensions. The ROMS model is a computational tool that employs a free-surface approach utilizing horizontally curvilinear and vertical terrain-following coordinates to solve hydrostatic, incompressible, and primitive equation<sup>29</sup>.

The model was implemented within a domain encompassing the North Western Pacific region and its marginal seas, spanning 115°–161.9° E longitude and 15°–52° N latitude (schematic flow in Fig. 1a). The model grid had a horizontal interval of 1/10° and 40 vertical layers. The vertical resolution varied according to the topography and was enhanced in shallow marginal seas. The model used monthly climatology initial temperature and salinity data in January from the World Ocean Atlas 2013<sup>30</sup>. The model incorporated a 10-year spin-up phase, initializing with surface and lateral boundary forcing data from 1982 to ensure equilibrium before analysis. Simple open ocean data assimilation (SODA) version 3.4.1 was used in this study for the lateral boundary condition, including the temperature, salinity, and zonal and meridional velocities<sup>31</sup>. The atmospheric surface forcing in our study was derived from the 6-hourly mean ERA5 variables, except for shortwave radiation, which was obtained from the daily mean ERA5 data. The European Center for Medium-Range Weather Forecasts generated a worldwide atmospheric reanalysis called ERA5<sup>32</sup>. Surface forcing variables, such as mean sea level pressure, 10 m winds, 2 m air temperature, specific humidity, and shortwave radiation, were employed. The surface heat flux was computed using a previously described bulk formula<sup>33</sup>. The lateral ocean boundary was incorporated with tides through the utilization of 10 tidal components (M2, S2, N2, K2, K1, O1, P1, Q1, Mf, and Mm), which were sourced from the TPXO7 ocean tide model<sup>34</sup>. This study used monthly mean river discharge data from 12 rivers located in the Bohai and Yellow Seas. Freshwater discharge from the Changjiang River was monitored at the Datong station, whereas the discharge data of the Han and Geum Rivers along the eastern coast of the YS were obtained from the National Institute of Environmental Research (NIER) and Hydrological Annual Report in Korea. Additionally, the discharge data for all other rivers along the Chinese and Korean coasts were sourced from the Global River Discharge Database<sup>35,36</sup>. The Earth Topography 1 arc-minute (ETOPO1) dataset was used to acquire topographic data, which were subsequently interpolated into model grid points<sup>37</sup>. The model was configured to integrate at 120-s intervals and generate daily results.

### Lagrangian trajectory model

The Lagrangian trajectory model employed in this study was OpenDrift, which is an open-source framework for simulating the trajectories and outcomes of drifting objects in the ocean<sup>38</sup>. OpenDrift tracks individual particles as they move with the ocean currents rather than modeling the flow itself. It is designed to be flexible and customizable, enabling users to configure the model to suit their specific needs and simulate the transport of particles three-dimensionally. A primary advantage of OpenDrift is its ability to integrate with other models and data sources.

While previous studies have provided valuable insights into general circulation patterns in EAMS using Eulerian analyses, these approaches are limited to resolving dynamic connectivity and material transport pathways<sup>1,39</sup>. Estimation of connectivity between straits using volume transport captures the balance of currents on barotropic adjustment timescales. However, such methods do not quantify how long materials take to transit between regions or how long they remain within specific areas. In contrast, the Lagrangian particle-tracking approach offers a more realistic and intuitive depiction of transport pathways, enabling estimation of actual travel times and residence times, and capturing the cumulative, time-integrated effects of circulation on material connectivity. Lagrangian particle tracking experiments have been conducted to investigate the transport of nutrients, microplastics, and other materials across shelf regions<sup>40–42</sup>.

In this study, particle trajectories were computed using a Lagrangian approach that integrates the advection-diffusion equation in three dimensions. The fundamental equation for updating particle positions at each time step  $\Delta t$  is given by:

$$X(t + \Delta t) = X(t) + U(X, t) \Delta t + \sqrt{2K\Delta t} \cdot \eta \quad (1)$$

where  $X$  represents the particle position vector  $(x, y, z)$ ,  $U(X, t)$  is the interpolated ocean velocity field obtained from the hydrodynamic model,  $K$  is the turbulent eddy diffusivity coefficient, and  $\eta$  is a vector of independent standard normal random variables accounting for subgrid-scale stochastic diffusion. The second term in right hand side describes deterministic advection driven by the resolved ocean currents, while the third term in right hand side represents random walk diffusion to simulate unresolved turbulent mixing. This approach enables the estimation of realistic pathways, travel times, and connectivity patterns of water parcels in the marine environment<sup>43</sup>. The turbulent eddy diffusivity coefficient  $K$  was set to 5 m<sup>2</sup>/s through comparison with the results of a ROMS online trajectory simulation (Supplementary Fig. 6).

In this study, we investigated the transport of particles from TS to KS using OpenDrift. The simulations utilized daily outputs from the regional three-dimensional ocean model, which provided detailed Eulerian velocity fields. Five hundred particles were dispersed uniformly at each depth from the surface to a depth of 70 m at 5-m intervals along a line traversing the TS, crossing the northern point of Taiwan at 121° E and 25° N and the coast of China at 120.18° E and 27° N (schematic flow in Fig. 1a).

The particles were instantaneously released on the first day of each month from 1982 to 2019, and their trajectories were tracked for 1 year at 1 day time intervals. Particles that reached the seafloor and coastline remained there unless they were lifted vertically to the seafloor level and transported back offshore by currents.

### Model validation

Model performance was assessed by comparing the simulated volume transport across the KS derived from the model with transport estimates determined from the empirical equation based on the sea level difference between the tide gauge stations in Busan, Korea, and Hakata, Japan (Supplementary Fig. 7a)<sup>44</sup>. The volume transport was approximately 2 Sv in winter and increased to approximately 3 Sv in late summer and fall. The model accurately simulated this seasonal cycle and the transport values, although it overestimated the fall transport by 0.3 Sv compared to the observations.

To examine the correlation between the observational data and model transport in the KS and TS, the transport scatter was plotted by comparing the transport volumes from the observations and model. For KS, observational data from a previous study<sup>44</sup> were used, whereas for TS, data from previous studies<sup>16,22,23</sup> were employed. Supplementary Fig. 7b shows the observed transport in the KS on the x-axis and the modeled transport on the y-axis. The correlation coefficient ( $R$ ) was 0.67, with a root mean square error (RMSE) of 0.32 Sv and a bias of 0.15 Sv. Despite the long comparison period from 1982 to 2018, the model demonstrated a strong correlation with observational data. Supplementary Fig. 7c shows a scatter plot comparing the model and observational transport in the TS. Although the number of observational datasets was smaller than that for KS, the correlation coefficient ( $R$ ) was 0.95, indicating a high level of agreement. The RMSE was 0.34 Sv, and the bias was  $-0.23$  Sv, demonstrating that the model provides reliable transport estimates for the Taiwan Strait. Comparison of the satellite-derived SSH and model SSH revealed that the model simulated the sea level well in the East China Sea (Supplementary Fig. 8).

To validate the model performance of TS transport, the modeled transport values were compared from 2009 to 2011 with observational estimates<sup>16</sup>. The modeled transport is within one standard deviation of the observation, indicating that the model reproduces the transport through the TS.

### Data availability

The World Ocean Atlas 2013 data are available from the National Centers for Environmental Information (NCEI) at <https://www.ncei.noaa.gov/products/world-ocean-atlas>. The ERA5 reanalysis data can be accessed through the Copernicus Climate Change Service (C3S) Climate Data Store at <https://essd.copernicus.org/articles/12/2097/2020/>. The TPXO7 tidal model data are available from the OSU Tidal Data Inversion website at [http://g.hyyb.org/archive/Tide/TPXO/TPXO\\_WEB/global.html](http://g.hyyb.org/archive/Tide/TPXO/TPXO_WEB/global.html). Discharge data referenced in [34–35] are available in their respective original publications. The ETOPO1 global relief model data are available from the National Geophysical Data Center (NGDC) at <https://www.ncei.noaa.gov/access/metadata/landing-page/bin/iso?id=gov.noaa.ngdc.mgg.dem:316>. Model configuration files and particle tracking data used in this study are available from the corresponding authors upon reasonable request.

Received: 17 May 2025; Accepted: 28 July 2025

Published online: 02 August 2025

### References

1. Teague, W. J. et al. Connectivity of the taiwan, cheju, and Korea Straits. *Cont. Shelf Res.* **23**, 63–77 (2003).
2. Jang, P. G. et al. Nutrient distribution and effects on phytoplankton assemblages in the Western korea/tsushima Strait. *N. Z. J. Mar. Freshw. Res.* **47**, 21–37 (2013).
3. Kodama, T., Morimoto, H., Igeta, Y. & Ichikawa, T. Macroscale-wide nutrient inversions in the subsurface layer of the Japan sea during summer. *J. Geophys. Res. Oceans.* **120**, 7476–7492 (2015).
4. Takikawa, T., Morimoto, A. & Onitsuka, G. Subsurface nutrient maximum and submesoscale structures in the Southwestern Japan sea. *J. Oceanogr.* **72**, 529–540 (2016).
5. Kwon, H. K. et al. Significant and Conservative long-range transport of dissolved organic nutrients in the Changjiang diluted water. *Sci Rep* **8**, (2018).
6. Shibano, R., Morimoto, A., Takayama, K., Takikawa, T. & Ito, M. Response of lower trophic ecosystem in the Japan sea to horizontal nutrient flux change through the Tsushima Strait. *Estuar Coast Shelf Sci* **229**, (2019).

7. Tian, Y., Kidokoro, H. & Watanabe, T. Long-term changes in the fish community structure from the Tsushima warm current region of the Japan/East Sea with an emphasis on the impacts of fishing and climate regime shift over the last four decades. *Prog Oceanogr.* **68**, 217–237 (2006).
8. Tian, Y., Kidokoro, H., Watanabe, T. & Iguchi, N. The late 1980s regime shift in the ecosystem of Tsushima warm current in the Japan/East Sea: evidence from historical data and possible mechanisms. *Prog Oceanogr.* **77**, 127–145 (2008).
9. Tian, Y., Kidokoro, H. & Fujino, T. Interannual-decadal variability of demersal fish assemblages in the Tsushima warm current region of the Japan Sea: impacts of climate regime shifts and trawl fisheries with implications for ecosystem-based management. *Fish. Res.* **112**, 140–153 (2011).
10. Tu, C. Y., Tian, Y. & Hsieh, C. H. Effects of climate on temporal variation in the abundance and distribution of the demersal fish assemblage in the Tsushima warm current region of the Japan Sea. *Fish. Oceanogr.* **24**, 177–189 (2015).
11. NIFS. Jellyfish information center. (2024). <https://www.nifs.go.kr/jelly/main.jelly>
12. Kim, K. R., Cho, Y. K., Kang, D. J. & Ki, J. H. The origin of the Tsushima current based on oxygen isotope measurement. *Geophys. Res. Lett.* **32**, 1–4 (2005).
13. Liu, Z. et al. Progress on circulation dynamics in the East China sea and Southern yellow sea: origination, pathways, and destinations of shelf currents. *Prog. Oceanogr.* **193**, (2021).
14. Qi, J., Yin, B., Zhang, Q., Yang, D. & Xu, Z. Seasonal variation of the Taiwan warm current water and its underlying mechanism. *Chin. J. Oceanol. Limnol.* **35**, 1045–1060 (2017).
15. Cho, Y. K. et al. Connectivity among Straits of the Northwest Pacific marginal seas. *J. Geophys. Res. Oceans.* **114**, 1–12 (2009).
16. Chen, H. W. et al. Temporal variations of volume transport through the Taiwan Strait, as identified by three-year measurements. *Cont. Shelf Res.* **114**, 41–53 (2016).
17. Hu, Z. et al. Characterizing surface circulation in the Taiwan Strait during NE monsoon from geostationary ocean color imager. *Remote Sens. Environ.* **221**, 687–694 (2019).
18. Chang, P. H. & Isobe, A. A numerical study on the Changjiang diluted water in the yellow and East China seas. *J. Geophys. Res. Oceans.* **108**, 1–17 (2003).
19. Zhang, C., Huang, Y. & Ding, W. Enhancement of Zhe-Min coastal water in the Taiwan Strait in winter. *J. Oceanogr.* **76**, 197–209 (2020).
20. Lian, E. et al. Kuroshio subsurface water feeds the wintertime Taiwan warm current on the inner East China sea shelf. *J. Geophys. Res. Oceans.* **121**, 4790–4803 (2016).
21. Kim, C. S. et al. Interannual variation of freshwater transport and its causes in the Korea Strait: A modeling study. *J. Mar. Syst.* **132**, 66–74 (2014).
22. Jan, S., Sheu, D. D. & Kuo, H. M. Water mass and throughflow transport variability in the Taiwan Strait. *J. Geophys. Res. Oceans* **111**, (2006).
23. Liu, K. K., Tang, Y., Gong, G. C., Chen, L. Y. & Shiah, F. K. Cross-shelf and along-shelf nutrient fluxes derived from flow fields and chemical hydrography observed in the Southern East China sea off Northern Taiwan. *Cont. Shelf Res.* **20**, 493–523 (2000).
24. Dong, X. Influences of the Pacific decadal oscillation on the East Asian summer monsoon in non-ENSO years. *Atmospheric Sci. Lett.* **17**, 115–120 (2016).
25. Zhou, C., Wu, L., Wang, C. & Cao, J. Shifted relationship between the Pacific decadal oscillation and Western North Pacific tropical cyclogenesis since the 1990s. *Environ. Res. Lett.* **19**, (2024).
26. Zhang, Y., Zhao, Z., Liao, E. & Jiang, Y. ENSO and PDO-related interannual and interdecadal variations in the wintertime sea surface temperature in a typical subtropical Strait. *Clim. Dyn.* **59**, 3359–3372 (2022).
27. Bae, H. J. et al. An Estimation of ocean surface heat fluxes during the passage of typhoon at the Ieodo ocean research station: typhoon Lingling case study 2019. *Asia Pac. J. Atmos. Sci.* **58**, 305–314 (2022).
28. Tang, H. S. et al. Positive feedback between the negative phase of interannual component of the Pacific decadal oscillation and La Niña. *Clim. Dyn.* <https://doi.org/10.1007/s00382-024-07346-4> (2024).
29. Shchepetkin, A. F. & McWilliams, J. C. The regional oceanic modeling system (ROMS): A split-explicit, free-surface, topography-following-coordinate oceanic model. *Ocean Model. (Oxf)*. **9**, 347–404 (2005).
30. Levitus, S. et al. The world ocean database. (2014). <http://www.nodc.noaa.gov/>
31. Carton, J. A. & Giese, B. S. A reanalysis of ocean climate using simple ocean data assimilation (SODA). *Mon Weather Rev.* **136**, 2999–3017 (2008).
32. Hersbach, H. et al. The ERA5 global reanalysis. *Q. J. R. Meteorol. Soc.* **146**, 1999–2049 (2020).
33. Fairall, C. W., Bradley, E. F., Hare, J. E., Grachev, A. A. & Edson, J. B. *Bulk Parameterization of Air-Sea Fluxes* (Updates and Verification for the COARE Algorithm, 2003).
34. Egbert, G. D. & Erofeeva, S. Y. Efficient inverse modeling of barotropic ocean tides. (2002).
35. Vörösmarty, C. J., Fekete, B. M. & Tucker, B. A. River discharge database version 1.0 (RivDIS v1.0). *Technical Documents Hydrology Series 0-6*, (1998).
36. Wang, Q., Guo, X. & Takeoka, H. Seasonal variations of the yellow river plume in the Bohai sea: A model study. *J. Geophys. Res. Oceans* **113**, (2008).
37. Amante, C. & Eakins, B. W. ETOPO1 1 Arc-minute global relief model: Procedures, data sources and analysis. NOAA technical memorandum NESDIS NGDC-24 19 (2009). <https://doi.org/10.1594/PANGAEA.769615>
38. Dagestad, K. F., Röhrs, J., Breivik, O. & Ådlandsvik, B. OpenDrift v1.0: A generic framework for trajectory modelling. *Geosci. Model. Dev.* **11**, 1405–1420 (2018).
39. Lee, H. J. & Chao, S. Y. A climatological description of circulation in and around the East China sea. *Deep Sea Res. 2 Top. Stud. Oceanogr.* **50**, 1065–1084 (2003).
40. Ser-Giacomi, E., Martinez-Garcia, R., Dutkiewicz, S. & Follows, M. J. A Lagrangian model for drifting ecosystems reveals heterogeneity-driven enhancement of marine plankton blooms. *Nat Commun* **14**, (2023).
41. Bigdeli, M., Mohammadian, A., Pilechi, A. & Taheri, M. Lagrangian modeling of Marine microplastics fate and transport: The State of the science. *J. Marine Sci. Eng.* **10** Preprint at (2022). <https://doi.org/10.3390/jmse10040481>
42. Liang, J. H. et al. Including the effects of subsurface currents on buoyant particles in Lagrangian particle tracking models: model development and its application to the study of riverborne plastics over the Louisiana/Texas shelf. *Ocean Model. (Oxf)* **167**, (2021).
43. North, E. W., Hood, R. R., Chao, S. Y. & Sanford, L. P. Using a random displacement model to simulate turbulent particle motion in a baroclinic frontal zone: A new implementation scheme and model performance tests. *J. Mar. Syst.* **60**, 365–380 (2006).
44. Shin, H. R. et al. Long-term variation in volume transport of the Tsushima warm current estimated from ADCP current measurement and sea level differences in the Korea/Tsushima Strait. *J. Mar. Syst.* **232**, (2022).

## Acknowledgements

This work was funded by the Korea Meteorological Administration Research and Development Program under Grant (RS-2024-00404973), the Institute for Basic Science (IBS) in Republic of Korea under IBS-R028-D1, the National Research Foundation of Korea (NRF) grant funded by the Korea government (Ministry of Science and ICT) (No. RS-2024-00405801), and Korea Institute of Marine Science & Technology Promotion (KIMST) funded by the Ministry of Oceans and Fisheries (RS-2022-KS221544).

### Author contributions

S.-T.L. and Y.-Y.K. analyzed the data and contributed to writing the manuscript, with S.-T.L. drafting the main text and Y.-Y.K. focusing on the results and discussion sections. The research topic was proposed by S.-T.L. and Y.-J.T., who also contributed to data analysis and writing parts of the manuscript. S.C. and Y.-K.C. provided the data used in the study, and Y.-K.C. reviewed and revised the manuscript. All authors reviewed the final version of the manuscript.

### Funding

This work was funded by the Korea Meteorological Administration Research and Development Program under Grant (RS-2024-00404973), the Institute for Basic Science (IBS) in Republic of Korea under IBS-R028-D1, the National Research Foundation of Korea (NRF) grant funded by the Korea government (Ministry of Science and ICT) (No. RS-2024-00405801), and Korea Institute of Marine Science & Technology Promotion (KIMST) funded by the Ministry of Oceans and Fisheries (RS-2022-KS221544).

### Declarations

#### Competing interests

The authors declare no competing interests.

#### Additional information

**Supplementary Information** The online version contains supplementary material available at <https://doi.org/10.1038/s41598-025-13861-z>.

**Correspondence** and requests for materials should be addressed to Y.-Y.K. or Y.-J.T.

**Reprints and permissions information** is available at [www.nature.com/reprints](http://www.nature.com/reprints).

**Publisher's note** Springer Nature remains neutral with regard to jurisdictional claims in published maps and institutional affiliations.

**Open Access** This article is licensed under a Creative Commons Attribution-NonCommercial-NoDerivatives 4.0 International License, which permits any non-commercial use, sharing, distribution and reproduction in any medium or format, as long as you give appropriate credit to the original author(s) and the source, provide a link to the Creative Commons licence, and indicate if you modified the licensed material. You do not have permission under this licence to share adapted material derived from this article or parts of it. The images or other third party material in this article are included in the article's Creative Commons licence, unless indicated otherwise in a credit line to the material. If material is not included in the article's Creative Commons licence and your intended use is not permitted by statutory regulation or exceeds the permitted use, you will need to obtain permission directly from the copyright holder. To view a copy of this licence, visit <http://creativecommons.org/licenses/by-nc-nd/4.0/>.

© The Author(s) 2025